Geophysical Research Letters

RESEARCH LETTER
10.1029/2018GL081730

Key Points:
- The first modeling effort is made for quasi-trapped electrons from CRAND in the inner radiation belt
- The simulated longitude distribution of quasi-trapped electrons from CRAND reproduces the observations
- Quantitative understanding of the CRAND-produced electrons in the inner belt and slot region is achieved based on the modeling effort

Supporting Information:
- Supporting Information S1

Correspondence to:
Z. Xiang,
xiangzheng@whu.edu.cn

Citation:
Xiang, Z., Li, X., Selesnick, R., Temerin, M. A., Ni, B., Zhao, H., et al. (2019). Modeling the quasi-trapped electron fluxes from cosmic ray albedo neutron decay (CRAND). *Geophysical Research Letters*, *46*, 1919–1928. https://doi.org/10.1029/2018GL081730

Received 17 DEC 2018
Accepted 28 JAN 2019
Accepted article online 30 JAN 2019
Published online 21 FEB 2019

©2019. American Geophysical Union. All Rights Reserved.

Modeling the Quasi-Trapped Electron Fluxes From Cosmic Ray Albedo Neutron Decay (CRAND)

Zheng Xiang[1,2], Xinlin Li[2,3], R. Selesnick[4], M. A. Temerin[5], Binbin Ni[1], Hong Zhao[2], Kun Zhang[2,3], and Leng Ying Khoo[2,3]

[1]Department of Space Physics, School of Electronic Information, Wuhan University, Wuhan, China, [2]Laboratory for Atmospheric and Space Physics, University of Colorado Boulder, Boulder, Colorado, USA, [3]Department of Aerospace Engineering Sciences, University of Colorado Boulder, Boulder, Colorado, USA, [4]Space Vehicles Directorate, Air Force Research Laboratory, Albuquerque, New Mexico, USA, [5]Space Sciences Laboratory, University of California, Berkeley, California, USA

Abstract Recently, cosmic ray albedo neutron decay (CRAND) has been identified as the main source of relativistic electrons measured at the inner edge of inner radiation belt. Here we introduce a drift-source model that includes azimuthal drift and a CRAND electron source to simulate the quasi-trapped electron distribution measured by the DEMETER satellite during 20–30 April 2010. The simulated longitude distribution of quasi-trapped electron fluxes at the inner edge of inner radiation belt successfully reproduces the DEMETER observations, confirming CRAND as the main source for these electrons. Furthermore, a comparison of the energy spectrum and the L distribution of the quasi-trapped relativistic electrons between simulations and observations further suggests that CRAND is likely the dominant source for 300–700-keV quasi-trapped electrons at $L < 2$ and $L \approx 3$.

Plain Language Summary Cosmic rays are mostly high-energy protons origin form supernovae in our galaxy. By interacting with neutral atoms in the Earth's upper atmosphere, cosmic rays can produce albedo neutrons with a mean lifetime of 887 s. An albedo neutron decays into a proton, an electron, and an antineutrino. This process is called cosmic ray albedo neutron decay, or CRAND. Li et al. (2017; https://doi.org/10.1038/nature24642) find that quasi-trapped electrons near the inner edge of the inner radiation belt measured by the Colorado Student Space Weather Experiment CubeSat are CRAND-produced. CRAND-produced electrons can accumulate during the drift and electron flux increase with longitude before reaching South Atlantic Anomaly. In return, the quasi-trapped electron fluxes can be used to infer the neutron density in the near-Earth space. Here we report a modeling study to reproduce this drift accumulation process.

1. Introduction

Energetic electrons in the Earth's radiation belts can be classified into three categories: untrapped (lifetime less than a bounce period), quasi-trapped (lifetime greater than a bounce time period but less than a drift time period), and trapped (lifetime greater than a drift time period). Quasi-trapped electrons have equatorial pitch angles (PA) between the local bounce loss cone (BLC) and the maximum BLC over all longitudes on their drift shell, and these electrons eventually precipitate into the atmosphere when they drift into the South Atlantic Anomaly (SAA) region. Low Earth orbit (LEO) satellites can measure all the three categories of electrons (e.g., Li et al., 2015; Zhao & Li, 2013). Using these LEO satellite observations, drift-diffusion models have been developed to quantify the precipitation loss of radiation belt electrons under different geomagnetic conditions (Pham et al., 2017; Selesnick, 2006; Selesnick et al., 2003; Tu et al., 2010).

Cosmic rays are mostly high-energy protons that are likely produced by supernova in our galaxy (e.g., Blasi, 2013). By interacting with neutral atoms in the Earth's upper atmosphere, cosmic rays can produce albedo neutrons with a mean lifetime of 887 s. An albedo neutron decays into a proton, an electron, and an antineutrino. This process is called cosmic ray albedo neutron decay, or CRAND. Most of the neutron kinetic energy is transferred to the proton, while the combined electron and neutrino kinetic energy is mostly from the binding energy (~0.782 MeV) and follows the β-decay spectrum (e.g., Selesnick, 2015). CRAND was identified as an important source for the inner proton radiation belt six decades ago (Kellogg, 1959; Selesnick et al., 2014; Singer, 1958), but not as a significant source of trapped electrons (Lenchek et al., 1961; Walt & Farley,

1976). Recently, relativistic electrons near the inner edge of the inner radiation belt were measured by the Colorado Student Space Weather Experiment CubeSat (Li et al., 2012, 2013) and identified as CRAND-produced (Li et al., 2017). The study further inferred the neutron density in the near-Earth space, based on the measured CRAND-produced electrons, to be ~$2 \times 10^{-9}/\mathrm{cm}^3$ (Li et al., 2017), which is comparable to earlier theoretical estimates (Hess et al., 1961). These new findings suggest that CRAND also contributes to the trapped electrons at lower L values, and thus, the dynamics of the inner radiation belt electrons needs to be revisited.

Here we report the first modeling effort on the CRAND-produced quasi-trapped electrons in the inner belt. It is a drift-source model to simulate the quasi-trapped electrons measured by the DEMETER satellite. The derivation of the equatorial pitch angle distribution of the CRAND-produced electrons and the description of the drift-source model are given in section 2. In section 3 we compare the simulated results with observations and investigate the energy spectrum and L dependence of the CRAND-produced electrons. We discuss and summarize our results in section 4.

2. Model Description

2.1. Equatorial Pitch Angle Distribution of the CRAND Electron Source

To evaluate quasi-trapped electrons from CRAND in near-Earth space, we first derive their equatorial pitch angle distribution. We assume that the spatial distribution of the electron injection rate (q) from CRAND is given by equation (1) of Lenchek et al. (1961):

$$q(r,\lambda,E) = \frac{n\varphi(E)}{4\pi T_n} = q_0(R_E/r)^{2.7}\left(3-2\cos^2\lambda\right)\varphi(E), \tag{1}$$

where $q(r,\lambda,E)$ is the electron injection rate that is assumed to be isotropic at each point in space, n is the neutron density, $T_n = 887s$ is the mean neutron lifetime, R_E is the radius of the Earth, r is the geocentric distance, λ is the geomagnetic latitude, $\varphi(E)$ is the neutron β-decay spectrum (see equation (4) of Selesnick, 2015), and q_0 is $3.7 \times 10^{-13}\mathrm{cm}^{-3}\mathrm{s}^{-1}\mathrm{ster}^{-1}$ from Lenchek et al. (1961). Note that the electron injection rate in equation (1) is longitude independent. Averaging the electron injection rate q over an electron spiral path S in a dipole magnetic field gives the equatorial pitch angle distribution of CRAND electrons (Lenchek et al., 1961, equations (17) and (20)):

$$\overline{q} = \int q\left(S'\right)dS/\int dS \simeq \frac{q_0\varphi(E)}{L^{2.7}\sin\alpha_{\mathrm{eq}}}, \tag{2}$$

where the integrations are carried out from the equatorial plane to the mirror point of the corresponding equatorial pitch angle. Here α_{eq} is the equatorial pitch angle and L is the radial distance in R_E at the equator if Earth's magnetic field is approximated as a dipole. The unit of $\overline{q}$ is $\mathrm{cm}^{-3}\ \mathrm{ster}^{-1}\ \mathrm{s}^{-1}\ \mathrm{MeV}^{-1}$.

The relationship between the CRAND electron source rate S_e and $\overline{q}$ is (Hess et al., 1961)

$$S_e = \overline{q}v \simeq \frac{q_0\varphi(E)v}{L^{2.7}\sin\alpha_{\mathrm{eq}}}, \tag{3}$$

where v is the electron speed and the unit of S_e is $\mathrm{cm}^{-3}\mathrm{ster}^{-1}\mathrm{s}^{-1}\mathrm{MeV}^{-1}$. The relationships between neutron density n, S_e, and $\overline{q}$ are derived in the supporting information.

Figure 1a shows the variation of S_e as a function of the equatorial pitch angle for 250-keV electrons at the indicated three specific L shells, and Figure 1b shows the variation of S_e as a function of electron kinetic energy at L = 1.5 for the three indicated equatorial pitch angles. It is evident that the value of S_e is dependent on energy and L, while the dependence on the equatorial pitch angle is relatively weak in the 60°–90° range. These results are similar to S_e evaluated by Monte Carlo simulations of cosmic ray interactions in the atmosphere (see Selesnick, 2015, Figure 2, although a significantly smaller q_0 value was implicitly assumed there).

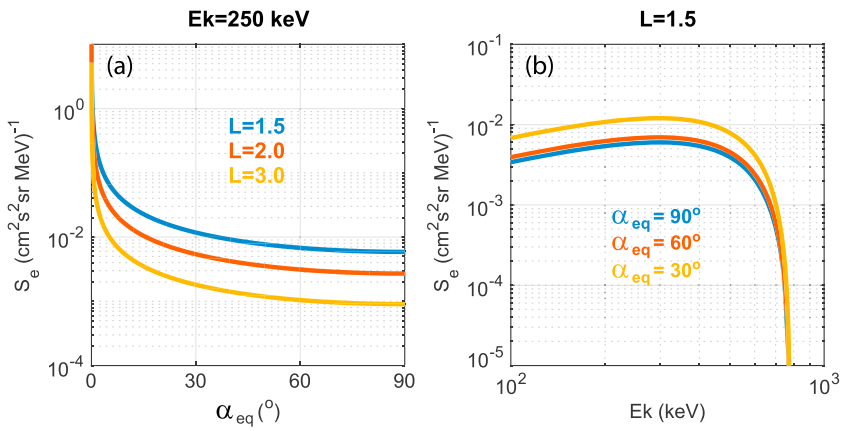

Figure 1. (a) The CRAND electron source rate S_e as a function of equatorial pitch angle for 250-keV electrons at the three indicated specific L shells. (b) S_e as a function of electron kinetic energy at L = 1.5 for the three indicated equatorial pitch angles.

2.2. Drift-Source Model

Here we assume that the quasi-trapped electrons near the inner edge of Earth's inner radiation belt are from a CRAND source and loss into the atmosphere at the SAA (Li et al., 2017). The drift-source model, for a given L shell and kinetic energy, is governed by the following equation (similar to equation (1) of Selesnick (2006)):

$$\frac{\partial f}{\partial t} + \omega_d \frac{\partial f}{\partial \phi} = \frac{S_e}{p^2}, \tag{4}$$

where ω_d is the bounce-averaged drift frequency, p is the electron momentum, f is the bounce-averaged electron phase space density as a function of α_{eq}, ϕ is the drift phase or geomagnetic longitude, and t is the time.

Since the relationship between electron flux J and electron phase space density f is

$$f = \frac{J}{p^2}, \tag{5}$$

Combining equations (4) and (5) gives

$$\frac{\partial J}{\partial t} + \omega_d \frac{\partial J}{\partial \phi} = S_e. \tag{6}$$

To evaluate the fluxes of quasi-trapped CRAND-produced electrons, we first assume that J is 0 at $t = 0$. In the model, there are 900 grid points in α_{eq} and 360 grid points in ϕ. A periodic boundary condition is adopted in ϕ. During each time step, we first move the fluxes in ϕ to simulate the drift process, which means that the electron fluxes at ϕ=360° in old matrix become $\phi = 1°$ in new matrix, electron fluxes at $\phi = 1°$ in old matrix become $\phi = 2°$ in new matrix, ..., and electron fluxes at $\phi = 359°$ in old matrix become $\phi = 360°$ in new matrix. Then adding on electron fluxes from CRAND ($\Delta t \bullet S_e$) at different pitch angles and longitudes. Here we assume that ω_d is the same for electrons with different equatorial pitch angle and at different geomagnetic longitudes, which is not true in nondipolar magnetic field (see Selesnick, 2012, Figure 1). We also assume that the S_e is constant during the simulation time period, since the intensity of cosmic ray is relatively stable and only modulated by solar cycle (Cane et al., 1999). The differences due to these assumptions are insignificant and the simulation results will not be changed significantly. The boundary condition is $J = 0$ at the edge of the BLC, which means that the BLC is empty. There is no boundary condition at PA = 90°; it just updates at every time step. Figure 2 shows the simulated 250-keV electron flux as a function of equatorial pitch angle and geomagnetic longitude at different times. The 90° equatorial pitch angle in Figure 2 corresponds to the position of minimum magnetic field strength at the local geomagnetic longitude based on the International Geomagnetic Reference Field model (year = 2010; Finlay et al., 2010). The L values

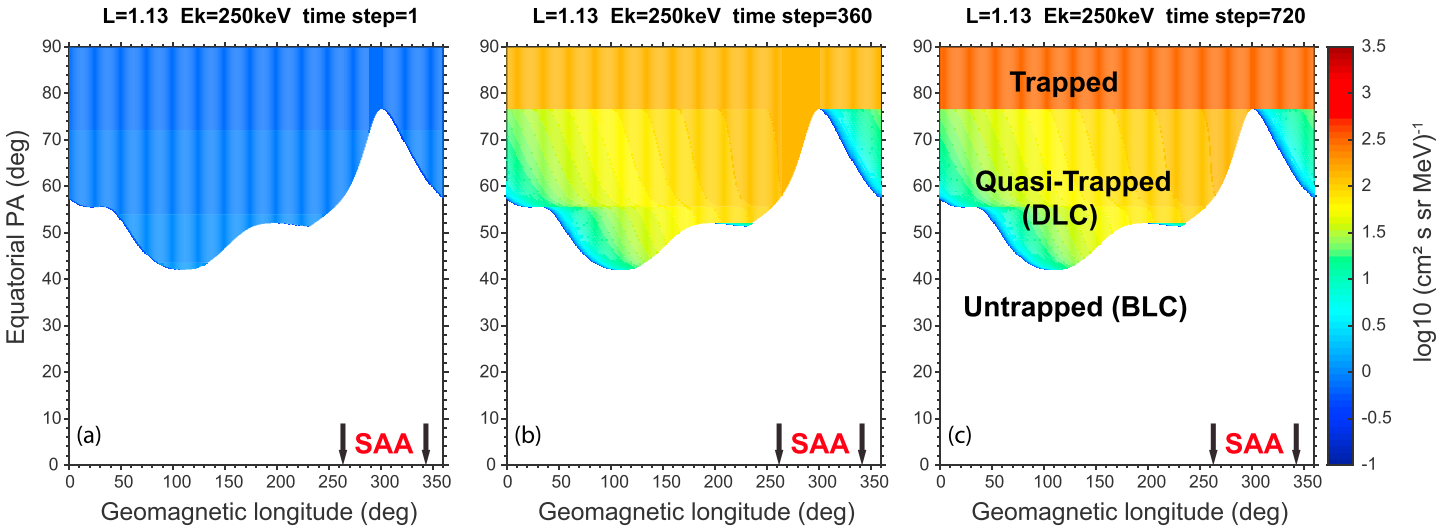

Figure 2. The simulated electron flux (color-coded) as a function of equatorial pitch angle and geomagnetic longitude after different time steps: (a) One time step (drift one degree in longitude), (b) 360 time steps (one drift time period), and (c) 720 time steps (two drift time periods). The white parts represent the bounce loss cone.

in the figure are McIlwain L (McIlwain, 1961). Electrons inside the BLC have the mirror points below 100 km in at least one hemisphere and are shown as blank in the figure. The magnetic field strength at 100-km altitude and at the geomagnetic equator are used to calculate the corresponding equatorial pitch angles of electrons mirroring at 100 km (e.g., Summers et al., 2007):

$$\sin^2(\alpha) = B\sin^2(\alpha_{eq})/B_{eq}, \tag{7}$$

where α is the local pitch angle, α_{eq} is the equatorial pitch angle, B is the local magnetic field, and B_{eq} is the equatorial magnetic field. The longitudinal dependence of the BLC in Figure 2 is due to the nondipolar nature of Earth's magnetic field. The electron flux in the BLC is set to zero. The electron drift direction is eastward (from left to right in Figure 2), and CRAND produces electrons at all longitudes simultaneously. Electrons with pitch angles greater than the largest BLC across all longitudes do not precipitate and are considered as stably trapped (e.g., greater than 77° equatorial pitch angle in Figure 2). Electrons in the drift loss cone (DLC) with equatorial pitch angles smaller than the largest BLC but larger than local BLC drift eastward, completing multiple bounces before precipitating into the SAA, and are considered as quasi-trapped (Selesnick, 2006).

After one time step, which means that the electrons drift 1° in geomagnetic longitude, the PA-longitude plot of J for 250-keV electrons at L = 1.13 is shown in Figure 2a. The CRAND-produced electron fluxes after one and two drift periods are shown in Figures 2b and 2c, respectively. We can see that the quasi-trapped electron fluxes at time step = 360 are the same as at time step = 720 because the CRAND source balances the drift loss, while the trapped electron fluxes increase as time increases.

3. Event Study

3.1. Modeling CRAND Electron Fluxes Measured by a LEO Satellite

Based on the drift-source model described in section 2, we compared the simulated electron fluxes with observations from the DEMETER satellite, which was launched into a Sun-synchronous orbit of 710-km altitude and 98.3° inclination on 29 June 2004 (Sauvaud et al., 2006). The Instrument for the Detection of Particles onboard DEMETER provides high-energy resolution (~18 keV) and time resolution (4 s) electron fluxes, which are ideal for inner belt electron studies. The quasi-trapped electrons measured by the DEMETER satellite at L = 1.13–1.15 during 20–30 April 2010 had been identified as being from CRAND (see Extended Data Figure 1 of Li et al. (2017)). The *Dst* index stayed above −37 nT during this time

period, showing a relatively quiet geomagnetic environment. Accordingly, we use this time period for our simulations and comparative analysis.

Figure 3 shows the simulation results from the drift-source model and observations from the DEMETER satellite during 20–30 April 2010 for four cases: (a–c) L = 1.08, E_k = 259.8 keV; (d–f) L = 1.08, E_k = 509 keV; (g–i) L = 1.13, E_k = 259.8 keV; and (j–l) L = 1.13, E_k = 509 keV. The green and blue colors in Figure 3 indicate the southern and northern hemispheres, respectively. Note that corrected geomagnetic coordinates are used in both simulations and observations, which defines the geomagnetic equator as the position of minimum magnetic field strength along each field line. The blue and green circle points in the drift-source model simulation results (Figures 3a, 3d, 3g, and 3j) are the equatorial pitch angles of electrons measured by the Instrument for the Detection of Particles instrument, which incorporate real satellite positions and detector looking directions during 20–30 April 2010. The detailed calculations of the blue/green circles points can be found in the supporting information. There are only quasi-trapped electrons at L = 1.08 (Figures 3a and 3d) since the minimum altitudes of equatorially mirroring electrons at L = 1.08 is below 100 km due to the off-center feature of Earth's magnetic field (see Li et al., 2017, Figure 2) while there are some trapped electrons at L = 1.13 (Figures 3g and 3j). Here we simulated 10 drift time periods (time step = 3,600) to make the simulated trapped electron fluxes comparable to observations, while the modeled quasi-trapped electron fluxes stay unchanged after one drift period.

From satellite observations, we observe that electron fluxes increase with longitude before reaching the SAA region, during which electron fluxes in the southern hemisphere (green color) are normally higher than those in the northern hemisphere (blue color) except for longitudes around [150°, 200°], where the geomagnetic field magnitude in the northern hemisphere is lower than that at the southern conjugate point, known as the North Pacific Anomaly (e.g., Zhang et al., 2017). The bump in electron fluxes around 50° longitudes (see Figures 3b and 3c) is due to the shape of bounce loss cone versus longitude curve in that region (see Figure 3a). These electron flux distribution features in the third column of Figure 3 are well reproduced by our modeling results in the second column. However, we note that the simulated electron fluxes are somewhat higher than the DEMETER observations, possibly due to the inaccuracy of neutron density distribution in equation (1). The good agreement between the simulation results and satellite observations for the longitudinal distribution of electron fluxes suggests that the drift-source model describes the dynamics of CRAND electrons in the drift loss cone well. This also serves as another solid evidence that the energetic electron at the inner edge of inner radiation belt is indeed CRAND-produced.

3.2. Energy Spectrum and L Dependence of CRAND Electron Fluxes

In the above section, we simulated quasi-trapped electron fluxes for four different cases using the drift-source model. To investigate the performance of the drift-source model at other energies and L values, we calculate the energy spectrum and L distribution of CRAND-produced electrons using drift-source model and compare them with DEMETER observations in this section. Figure 4 shows the energy spectrum of electron fluxes at six L values: (a) L = 1.08, (b) L = 1.13, (c) L = 1.5, (d) L = 2, (e) L = 2.5, and (f) L = 3 and the L distribution of electron fluxes at (g) E_k = 259.8 keV and (h) E_k = 509 keV. The green and blue colors indicate southern and northern hemispheres, respectively. The solid lines are from the simulations while the star points are obtained from satellite observations, although the blue and green solid lines are too close to be distinguished. We adjust q_0 values to get a better consistency between simulations and observations, which are indicated at the top of Figures 4a–4f. The q_0 value used to get the L dependences in Figures 4g and 4h is still $3.7 \times 10^{-13}\mathrm{cm}^{-3}\mathrm{s}^{-1}\mathrm{ster}^{-1}$, the original value from Lenchek et al. (1961) as described in section 2.

Close to the inner edge of inner radiation belt (L = 1.08, 1.13), the overall simulated energy spectrum of electron fits the observations from DEMETER quite well (Figures 4a and 4b) while the simulations only match well with observations at high energies at higher L (Figures 4c and 4d). This trend indicates that CRAND is the main source of quasi-trapped electrons at high energy ($E_k > 300$ keV) at L < 2 but not the main source of low-energy electrons ($E_k < 300$ keV) at L > 1.5. This is consistent with results of Zhang et al. (2019) that are derived purely based on observations. Possible sources of quasi-trapped electrons at lower energies are atmospheric collisions (Selesnick, 2012; Walt, 1964) or wave-particle interaction (Abel & Thorne, 1998; Lyons & Williams, 1975; Ni et al., 2013; Selesnick et al., 2013; Xiang et al., 2016), which can scatter trapped electrons into the drift loss cone. As the L value increases, the q_0 value used to adjust the simulation closer to

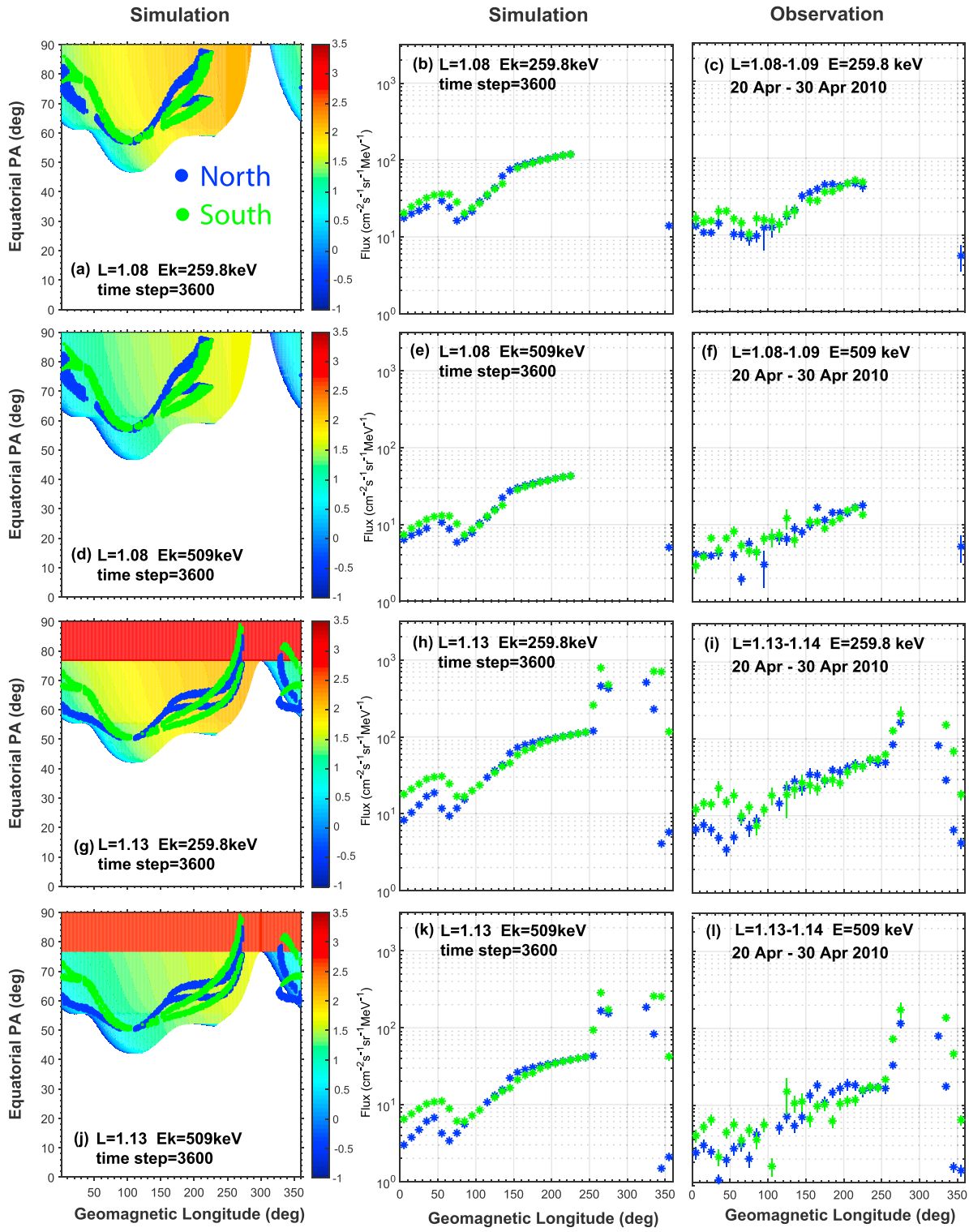

Figure 3. (first column) Simulated electron fluxes as a function of equatorial pitch angle and geomagnetic longitude. The blue and green points are equatorial pitch angles of electrons measured by the instrument which incorporates real satellite position and detector looking direction. We assume that all the electrons come from the center of the telescope. (second column) Simulated electron fluxes corresponding to the blue (green) points in first column panels. (third column) Electron flux observations from the DEMETER satellite, which are binned over 10° longitudes and averaged over the period of 20–30 April 2010. The error bars are in units of flux per square root of N, where N is the number of data points. The green and blue colors in Figure 3 indicate southern and northern hemispheres, respectively. Four cases are shown: (a–c) L = 1.08, E_k = 259.8 keV; (d–f) L = 1.08, E_k = 509 keV; (g–i) L = 1.13, E_k = 259.8 keV; and (j–l) L = 1.13, E_k = 509 keV.

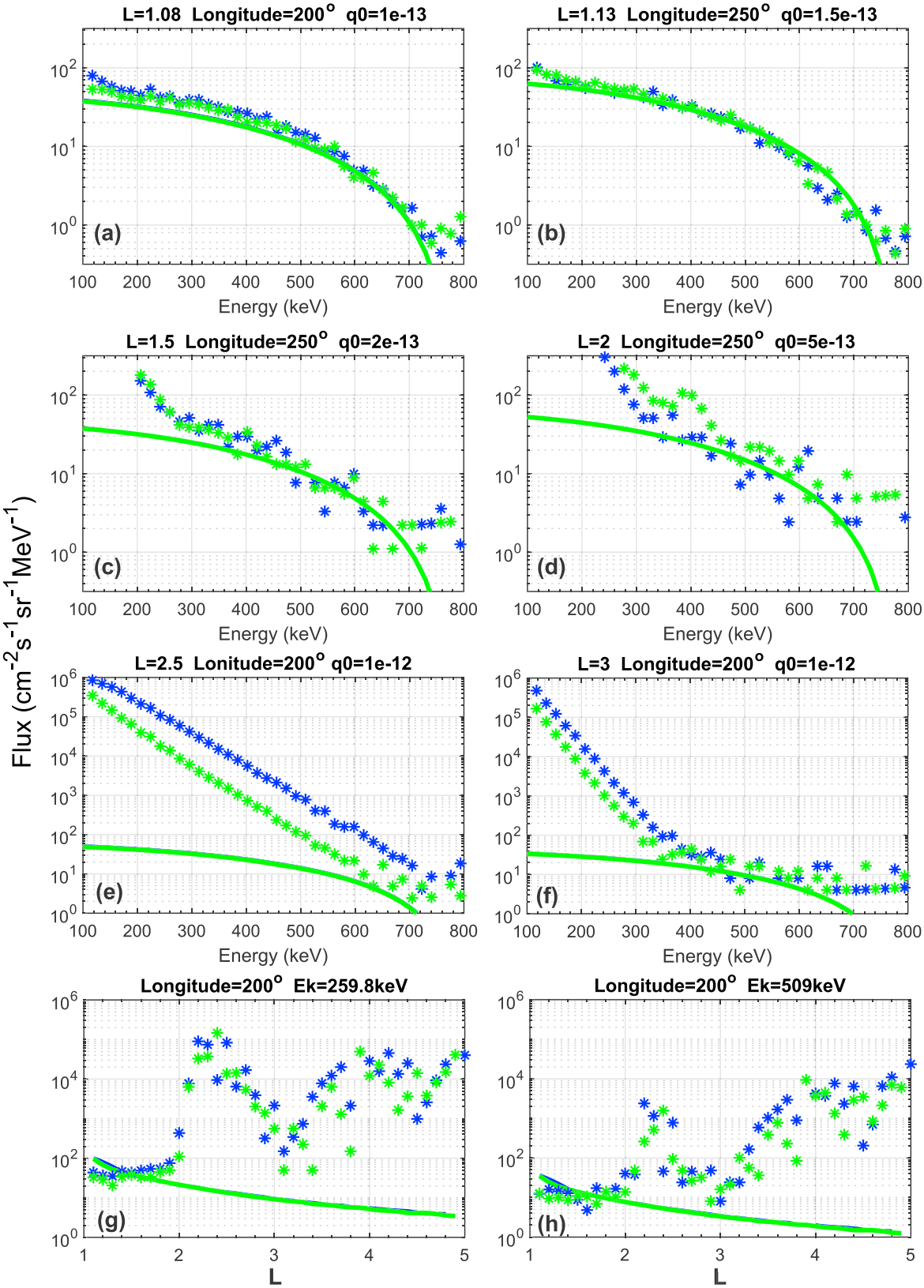

Figure 4. Electron energy spectra from simulation (solid lines) and observation (star points) during 20–30 April 2010 at six L values: (a) L = 1.08, (b) L = 1.13, (c) L = 1.5, (d) L = 2, (e) L = 2.5, and (f) L = 3. L dependence of electron fluxes from simulation (solid lines) and observation (star points) for two energies: (g) E_k = 259.8 keV and (h) E_k = 509 keV. The green and blue colors indicate southern and northern hemispheres, respectively.

observation also increases (see Figures 4a–4d), which means the source term S_e in equation (4) needs to be enlarged at higher L, indicating that equation (1) from Lenchek et al. (1961) may underestimate the neutron density at higher L values. S_e in equation (4) is obtained under dipole magnetic field while the Earth's real magnetic field is nondipole, which may reduce the shell volume available for neutron decay at lower L, but increase it at higher L. Regarding the L dependency of quasi-trapped electrons, the simulation results are close to satellite observations at $L < 2$ and $L \approx 3$ for both energies (Figures 4g and 4h), indicating that CRAND is the main source of quasi-trapped electrons in these regions. The high quasi-trapped electron flux levels around L = 2.5 can be explained by the scattering effect of plasmaspheric hiss and lightning generated whistler wave on trapped electrons, which have different flux levels at L = 3 and L = 2.5. Based on previous statistics of lightning-generated whistler and plasmaspheric hiss waves together with plasma density, Mourenas et al. (2017) have shown that a much faster hiss wave-driven 300–700-keV electron loss is expected at L = 3 than at L = 2.5 during quiet periods. The corresponding 300–700-keV electron lifetimes are about 1–2 days at L = 3 versus ~5–20 days at L = 2.5. Figures 3a and 3e from Mourenas et al. (2017) show a negligible 300–700-keV trapped electron flux at L = 3 and a high flux at L = 2.5 after persistent quiet periods. This could explain the dominance of CRAND-produced quasi-trapped electrons above 300 keV at L = 3 but not at L = 2.5, where a high remaining flux of inward transported outer belt electrons can be continuously scattered toward the loss cone by lightning-generated whistler and plasmaspheric hiss waves (Meredith et al., 2007; Mourenas et al., 2017; Ni et al., 2014, 2017; Zhao et al., 2019). The energy spectrum analysis in Figure 4e also suggest that CRAND is not the main source of electrons at L = 2.5, since the observed electron energy spectra show an exponential distribution that is very different from the simulated energy spectra from CRAND. In contrast, the simulated energy spectrum of electron fits the observations from DEMETER well at 350–700 keV in Figure 4f, indicating that CRAND is likely the main source of 350–700-keV electrons at L = 3. Electron fluxes in the outer radiation belt (see $L > 3$ regions in Figures 4g and 4h) are orders of magnitude higher than simulated CRAND-produced electron fluxes, suggesting that the CRAND contribution is negligible in the outer radiation belt. It should be noted that different longitude cuts are selected at different panels in Figure 4. In this study, we prefer to compare simulations and observations with higher flux level, which can reduce the uncertainty of satellite measurements. Therefore, most panels choose longitude = 250° (closer to the west of SAA) for comparison. The reason why longitude = 200° is chosen at L = 1.08 is that there is no measurement from satellite at longitude = 250° at this low L (see Figures 3a–3c). To keep the consistence at different L values, longitude = 200° is also chosen in L distribution panels (Figures 4g and 4h). Figures 4e and 4f are displayed to support the conclusions from Figures 4g and 4h, so longitude = 200° is chosen.

4. Discussion and Conclusion

In this report, quasi-trapped electrons produced by CRAND have been simulated using the drift-source model and compared with DEMETER observations. The simulations are conducted to obtain the longitudinal distributions of electron fluxes at 259.8 and 509 keV for different L shells, L = 1.08 and L = 1.13. The good agreement between the simulations and the observations confirm that CRAND is the main source of quasi-trapped relativistic electrons at the inner edge of inner radiation belt. The effect of pitch angle and energy diffusion is not included in the simulations since these effects are expected to be insignificant at such low L regions over the time scales considered (Ma et al., 2017; Selesnick, 2016).

In addition, by investigating the energy spectrum and L dependences of CRAND electrons, we find that CRAND is the main source of quasi-trapped electrons at energies 300–700 keV at $L < 2$ and $L \approx 3$, where trapped electrons also exist. These new findings lead to some interesting questions: what role does CRAND play in trapped electron dynamics and how do the contributions of different responsible mechanisms vary with respect to the geomagnetic activity level? We note that the CRAND contribution is expected to be relatively steady while the trapped electron fluxes vary significantly for both the inner and outer belts. To answer these questions, both the source and loss mechanisms in these regions need to be analyzed, which will be investigated in our future studies.

Under both active and quiet geomagnetic environment, the energetic electrons at the inner edge of inner belt have been demonstrated from CRAND (Li et al., 2017; Zhang et al., 2019). Thus, at the inner edge of inner radiation belt, the drift-source model is expected to reproduce observations for both active and quiet periods

well. But for panels with higher L values in Figure 4, since injection dominates the electron dynamics in inner belt during active periods, it can be expected that the performance of drift-source model is better during quiet periods, but not as well during active periods.

The global distribution of neutron density is the most important input parameter for the drift-source model. In this study, the neutron density distribution model is adopted from the study of Lenchek et al. (1961), which shows some differences when compared with the simulation results and satellite observations (see Figure 4). Li et al. (2017) presented a method to infer the neutron density based on CRAND electron fluxes measured by LEO satellites, which can be used to acquire more reliable neutron density information in near-Earth space. However, the neutron density calculated in Li et al. (2017) is assumed uniform across different latitude. In future work, we intend to assume a latitudinal distribution of neutron density based on the method of Li et al. (2017) and then incorporate it into the drift-source model. A more realistic neutron density distribution is expected to further improve the simulation results.

Acknowledgments
This work was supported by NSF grant AGS 1443749 and NASA grant NNX15AF56G. BN acknowledges the support from NSFC grants 41674163, 41474141, and 41204120 and from the Hubei Province Natural Science Excellent Youth Foundation (2016CFA044). DEMETER data are publicly available at https://cdpp-archive.cnes.fr.

References

Abel, B., & Thorne, R. M. (1998). Electron scattering loss in Earth's inner magnetosphere, 1. Dominant physical processes. *Journal of Geophysical Research*, *103*(A2), 2385–2396. https://doi.org/10.1029/97JA02919

Blasi, P. (2013). The origin of galactic cosmic rays. *The Astronomy and Astrophysics Review*, *21*(1), 70. https://doi.org/10.1007/s00159-013-0070-7

Cane, H. V., Wibberenz, G., Richardson, I. G., & von Rosenvinge, T. T. (1999). Cosmic ray modulation and the solar magnetic field. *Geophysical Research Letters*, *26*(5), 565–568. https://doi.org/10.1029/1999GL900032

Finlay, C. C., Maus, S., Beggan, C. D., Bondar, T. N., Chambodut, A., Chernova, T. A., et al. (2010). International geomagnetic reference field: The eleventh generation. *Geophysical Journal International*, *183*(3), 1216–1230. https://doi.org/10.1111/j.1365-246X.2010.04804.x

Hess, W. N., Canfield, E. H., & Lingenfelter, R. E. (1961). Cosmic-ray neutron demography. *Journal of Geophysical Research*, *66*(3), 665–677. https://doi.org/10.1029/JZ066i003p00665

Kellogg, P. J. (1959). Van Allen radiation of solar origin. *Nature*, *183*(4671), 1295–1297. https://doi.org/10.1038/1831295a0

Lenchek, A. M., Singer, S. F., & Wentworth, R. C. (1961). Geomagnetically trapped electrons from cosmic ray albedo neutrons. *Journal of Geophysical Research*, *66*(12), 4027–4046. https://doi.org/10.1029/JZ066i012p04027

Li, X., Palo, S., Kohnert, R., Gerhardt, D., Blum, L., Schiller, Q., et al. (2012). Colorado student space weather experiment: Differential flux measurements of energetic particles in a highly inclined low earth orbit. In *Dynamics of the Earth's Radiation Belts and Inner Magnetosphere*, Geophysical Monograph Series (Vol. 199, pp. 385–404). Washington, DC: American Geophysical Union. https://doi.org/10.1029/2012GM001313

Li, X., Schiller, Q., Blum, L., Califf, S., Zhao, H., Tu, W., et al. (2013). First results from CSSWE CubeSat: Characteristics of relativistic electrons in the near-earth environment during the October 2012 magnetic storms. *Journal of Geophysical Research: Space Physics*, *118*, 6489–6499. https://doi.org/10.1002/2013JA019342

Li, X., Selesnick, R., Schiller, Q., Zhang, K., Zhao, H., Baker, D. N., & Temerin, M. A. (2017). Measurement of electrons from albedo neutron decay and neutron density in near-Earth space. *Nature*, *552*(7685), 382–385. https://doi.org/10.1038/nature24642

Li, X., Selesnick, R. S., Baker, D. N., Jaynes, A. N., Kanekal, S. G., Schiller, Q., et al. (2015). Upper limit on the inner radiation belt MeV electron intensity. *Journal of Geophysical Research: Space Physics*, *120*, 1215–1228. https://doi.org/10.1002/2014JA020777

Lyons, L. R., & Williams, D. J. (1975). The quiet time structure of energetic (35–560 keV) radiation belt electrons. *Journal of Geophysical Research*, *80*(7), 943–950. https://doi.org/10.1029/JA080i007p00943

Ma, Q., Mourenas, D., Li, W., Artemyev, A., & Thorne, R. M. (2017). VLF waves from ground-based transmitters observed by the Van Allen probes: Statistical model and effects on plasmaspheric electrons. *Geophysical Research Letters*, *44*, 6483–6491. https://doi.org/10.1002/2017GL073885

McIlwain, C. E. (1961). Coordinates for mapping the distribution of magnetically trapped particles. *Journal of Geophysical Research*, *66*(11), 3681–3691. https://doi.org/10.1029/JZ066i011p03681

Meredith, N. P., Horne, R. B., Glauert, S. A., & Anderson, R. R. (2007). Slot region electron loss timescales due to plasmaspheric hiss and lightning generated whistlers. *Journal of Geophysical Research*, *112*, A08214. https://doi.org/10.1029/2006JA012413

Mourenas, D., Ma, Q., Artemyev, A. V., & Li, W. (2017). Scaling laws for the inner structure of the radiation belts. *Geophysical Research Letters*, *44*, 3009–3018. https://doi.org/10.1002/2017GL072987

Ni, B., Bortnik, J., Thorne, R. M., Ma, Q., & Chen, L. (2013). Resonant scattering and resultant pitch angle evolution of relativistic electrons by plasmaspheric hiss. *Journal of Geophysical Research: Space Physics*, *118*, 7740–7751. https://doi.org/10.1002/2013JA019260

Ni, B., Hua, M., Zhou, R., Yi, J., & Fu, S. (2017). Competition between outer zone electron scattering by plasmaspheric hiss and magnetosonic waves. *Geophysical Research Letters*, *44*, 3465–3474. https://doi.org/10.1002/2017GL072989

Ni, B., Li, W., Thorne, R. M., Bortnik, J., Ma, Q., Chen, L., et al. (2014). Resonant scattering of energetic electrons by unusual low-frequency hiss. *Geophysical Research Letters*, *41*, 1854–1861. https://doi.org/10.1002/2014GL059389

Pham, K. H., Tu, W., & Xiang, Z. (2017). Quantifying the precipitation loss of radiation belt electrons during a rapid dropout event. *Journal of Geophysical Research: Space Physics*, *122*, 10,287–10,303. https://doi.org/10.1002/2017JA024519

Sauvaud, J. A., Moreau, T., Maggiolo, R., Treilhou, J. P., Jacquey, C., Cros, A., et al. (2006). High-energy electron detection onboard DEMETER: The IDP spectrometer, description and first results on the inner belt. *Planetary and Space Science*, *54*(5), 502–511. https://doi.org/10.1016/j.pss.2005.10.019

Selesnick, R. S. (2006). Source and loss rates of radiation belt relativistic electrons during magnetic storms. *Journal of Geophysical Research*, *111*, A04210. https://doi.org/10.1029/2005JA011473

Selesnick, R. S. (2012). Atmospheric scattering and decay of inner radiation belt electrons. *Journal of Geophysical Research*, *117*, A08218. https://doi.org/10.1029/2012JA017793

Selesnick, R. S. (2015). High-energy radiation belt electrons from CRAND. *Journal of Geophysical Research: Space Physics*, *120*, 2912–2917. https://doi.org/10.1002/2014JA020963

Selesnick, R. S. (2016). Stochastic simulation of inner radiation belt electron decay by atmospheric scattering. *Journal of Geophysical Research: Space Physics*, *121*, 1249–1262. https://doi.org/10.1002/2015JA022180

Selesnick, R. S., Albert, J. M., & Starks, M. J. (2013). Influence of a ground-based VLF radio transmitter on the inner electron radiation belt. *Journal of Geophysical Research: Space Physics*, *118*, 628–635. https://doi.org/10.1002/jgra.50095

Selesnick, R. S., Baker, D. N., Jaynes, A. N., Li, X., Kanekal, S. G., Hudson, M. K., & Kress, B. T. (2014). Observations of the inner radiation belt: CRAND and trapped solar protons. *Journal of Geophysical Research: Space Physics*, *119*, 6541–6552. https://doi.org/10.1002/2014JA020188

Selesnick, R. S., Blake, J. B., & Mewaldt, R. A. (2003). Atmospheric losses of radiation belt electrons. *Journal of Geophysical Research*, *108*(A12), 1468. https://doi.org/10.1029/2003JA010160

Singer, S. F. (1958). Trapped albedo theory of the radiation belt. *Physical Review Letters*, *1*(5), 181–183. https://doi.org/10.1103/PhysRevLet.1.181

Summers, D., Ni, B., & Meredith, N. P. (2007). Timescales for radiation belt electron acceleration and loss due to resonant wave-particle interactions: 1. Theory. *Journal of Geophysical Research*, *112*, A4206. https://doi.org/10.1029/2006JA011801

Tu, W., Selesnick, R., Li, X., & Looper, M. (2010). Quantification of the precipitation loss of radiation belt electrons observed by SAMPEX. *Journal of Geophysical Research*, *115*, A07210. https://doi.org/10.1029/2009JA014949

Walt, M. (1964). The effects of atmospheric collisions on geomagnetically trapped electrons. *Journal of Geophysical Research*, *69*(19), 3947–3958. https://doi.org/10.1029/JZ069i019p03947

Walt, M., & Farley, T. A. (1976). The physical mechanisms of the inner Van Allen belt. *Fundamentals of Cosmic Physics*, *2*, 1–110.

Xiang, Z., Ni, B., Zhou, C., Zou, Z., Gu, X., Zhao, Z., et al. (2016). Multi-satellite simultaneous observations of magnetopause and atmospheric losses of radiation belt electrons during an intense solar wind dynamic pressure pulse. *Annales de Geophysique*, *34*(5), 493–509. https://doi.org/10.5194/angeo-34-493-2016

Zhang, K., Li, X., Schiller, Q., Gerhardt, D., Zhao, H., & Millan, R. (2017). Detailed characteristics of radiation belt electrons revealed by CSSWE/REPTile measurements: Geomagnetic activity response and precipitation observation. *Journal of Geophysical Research: Space Physics*, *122*, 8434–8445. https://doi.org/10.1002/2017JA024309

Zhang, K., Li, X., Zhao, H., Schiller, Q., Khoo, L. Y., Xiang, Z., et al. (2019). Cosmic ray albedo neutron decay (CRAND) as a source of inner belt electrons: Energy spectrum study. *Geophysical Research Letters*, *46*. https://doi.org/10.1029/2018GL080887

Zhao, H., & Li, X. (2013). Modeling energetic electron penetration into the slot region and inner radiation belt. *Journal of Geophysical Research: Space Physics*, *118*, 6936–6945. https://doi.org/10.1002/2013JA019240

Zhao, H., Ni, B., Li, X., Baker, D. N., Johnston, W. R., Zhang, W., et al. (2019). Plasmaspheric hiss waves generate a reversed energy spectrum of radiation belt electrons. *Nature Physics*. https://doi.org/10.1038/s41567-018-0391-6